

## AGN star dynamics under the Influence of Outflow-Ambient Interactions

MUXIN LIU ,<sup>1,2</sup> LILE WANG ,<sup>2,1</sup> AND PENG PENG<sup>1,2</sup><sup>1</sup>Department of Astronomy, School of Physics, Peking University, Beijing 100871, China<sup>2</sup>Kavli Institute for Astronomy and Astrophysics, Peking University, Beijing 100871, China

## ABSTRACT

Stars with outflows interacting with ambient gas experience accelerations arising from the gravitational feedback induced by the interaction structure. In this work, three-dimensional (3D) local shearing box simulations are performed to investigate the dynamical evolution of a star with outflows embedded in the outer regions of an active galactic nucleus (AGN) disk. Two types of stellar wind are considered: isotropic winds and axisymmetric jets, along with variations in the radial pressure gradient profile. The results show that anti-friction enables AGN stars to acquire angular momentum from the ambient gas, resulting in outward migration away from the disk center. The formation and stability of the head-wind structure, which is crucial for maintaining anti-friction, are sensitive to both the strength of the stellar outflow and the radial pressure gradient of the disk gas. Once the head-wind structure is disrupted, the anti-friction effect ceases to operate effectively. A case study is also presented, focusing on a stellar-mass black hole (sBH) in an AGN disk. It is shown that jet material launched along the z-axis is confined to the trailing side of the object's motion by high gas inflow velocities, thereby activating anti-friction and inducing outward migration. If such an sBH migrates inward initially, the interplay between inward and outward migration may trap it at an equilibrium radius, potentially facilitating the formation and merger of black hole binaries.

*Keywords:* Stellar dynamics (1596), Active galactic nuclei(16), Stellar winds (1636), Stellar mass loss (1613), Dynamical friction (422), Stellar mass black holes(1611)

## 1. INTRODUCTION

The discovery of quasars marked a significant breakthrough in understanding the formation and evolution of galaxies (Schmidt 1963), revealing them as the most luminous members of active galactic nuclei (AGNs; Peterson 1997; Ho 2008). These AGNs are believed to be powered by the rapid accretion of matter onto supermassive black holes (SMBHs), where gravitational energy is efficiently released through accretion disks at high rates (Lynden-Bell 1969). Given their crucial role in AGNs, the structure and dynamics of these disks have been extensively studied since the pioneering work of Shakura & Sunyaev (1973).

Within AGN disks, the mechanisms governing the presence and motion of stars and compact stellar remnants have long been a focus of theoretical research. These objects enter AGN disks via at least two mech-

anisms. One mechanism involves *in-situ* formation: when an extended AGN accretion disk becomes self-gravitating, it may undergo fragmentation, leading to the birth of stars (Paczynski 1978; Kolykhalov & Syunyaev 1980; Shlosman & Begelman 1987; Goodman 2003; Jiang & Goodman 2011; Chen et al. 2023). This process preferentially produces massive stars, which can grow further through sustained accretion (Levin 2003; Goodman & Tan 2004; Dittmann & Miller 2020). The other mechanism is the stellar capture, during which stars originally orbiting near the galactic center may lose energy and angular momentum through repeated interactions with the AGN disk. Such dissipative processes, driven by hydrodynamic drag and the excitation of resonant density and bending waves, settle stars into circular, corotating orbits within the disk (Syer et al. 1991; Artymowicz et al. 1993; MacLeod & Lin 2020; Wang et al. 2024). This capture process is expected to be efficient within approximately 10 pc of the SMBH (Artymowicz et al. 1993; Just et al. 2012; Kennedy et al. 2016; Fabj et al. 2020; MacLeod & Lin 2020). Depending on the AGN's lifetime and disk properties, simula-

Corresponding author: Lile Wang  
lilew@pku.edu.cn

tions suggest that a few hundred stars could be captured over a period of about one million years (Panamarev et al. 2018; Fabj et al. 2020). Over longer timescales, approaching 100 million years, the number of captured stars could exceed  $10^4$  (Artymowicz et al. 1993).

Stars embedded in AGN disks (AGN stars) are expected to travel under conditions quite different from those in standard galactic environments. Due to the extreme temperatures and densities of AGN disks, these stars are subject to very different boundary conditions (BCs) than normal stars, which significantly influence their dynamical evolution. Consequently, the detailed dynamical evolution of AGN stars remains an open question. Proper modeling must account for their prolonged exposure to intense pressures, temperatures, and accretion rates. Several studies have explored various aspects of the dynamical behavior of AGN stars. Cantiello et al. (2021) introduced modifications to standard stellar dynamical evolution models to accommodate the extreme conditions present in different regions of AGN disks. Additionally, the dynamics of stellar-mass binary black holes in AGN disks have been examined by Li & Lai (2022, 2023, 2024), while Peng & Chen (2023); Peng et al. (2024) investigated the interaction between a gap-opening intermediate-mass-ratio inspiral (IMRI) and surrounding sBHs within an AGN disk. The high-density environment of AGN disks facilitates conditions where stars may exceed the Eddington limit, leading to the production of powerful outflows (Wang et al. 2021). However, existing studies have not yet addressed how stellar outflows influence the dynamical evolution of AGN stars. This work aims to incorporate the effects of outflows into the study of AGN star dynamics.

It is well acknowledged that a massive object moving through a gaseous medium experiences dynamical friction (Chandrasekhar & von Neumann 1942; Ostriker 1999; Edgar 2004), a key hydrodynamic drag mechanism involved in stellar capture. However, this scenario changes if the object launches strong winds. Gruzinov et al. (2020) demonstrate that when the wind velocity is sufficiently high, a large underdense region forms around the object, altering the net gravitational force exerted by the ambient gas. This effect can reverse the drag force, causing it to align with the object’s motion—a phenomenon known as anti-friction, where the object accelerates instead of decelerating. Li et al. (2020) employed hydrodynamic simulations to investigate how stellar outflows affect accretion rates and modify the strength of anti-friction. Moreover, Wang & Li (2022) studied anti-friction in binary systems using global 3D hydrodynamic simulations. Liu et al. further examined the role of anti-friction in the dynamical evolution of stars in open clus-

**Table 1.** Initial Properties of the Fiducial Model

Item	Value
<b>Disk Properties</b>	
$M$	$10^8 M_\odot$
$\rho_0$	$\sim 8 \times 10^{-12} \text{ g cm}^{-3}$
$c_{\text{iso}}$	$10^6 \text{ cm s}^{-1}$
$x_p$	90 AU
$v_{\text{acc}}^*$	0 cm s $^{-1}$
<b>Stellar Properties</b>	
$m$	$8 M_\odot$
$r_0$	$5000 R_{\text{sch}}$
$\dot{m}$	$\sim 3 \times 10^{-3} M_\odot \text{ yr}^{-1}$
$T_{\text{outflow}}$	$\sim 6 \times 10^4 \text{ K}$
$v_{\text{src}}$	$\sim 8 \times 10^7 \text{ cm s}^{-1}$
$r_{\text{soft}}/r_{\text{src}}$	$\sim 3$
Outflow Type $^\dagger$	Isotropic
<b>Simulation Parameters</b>	
$L_x, L_y, L_z$	75, 150, 75 AU
Resolution ( $N_x, N_y, N_z$ )	128, 256, 128
$t_{\text{evo}}$	15 $P$

NOTE— \*:  $v_{\text{acc}} = 0$  corresponds to a non-accreting disk.

$^\dagger$ : The fiducial model assumes an isotropic stellar outflow. Jet and no-outflow models are also discussed (see §3.3).

ters. Carrillo-Santamaría et al. (2025) investigate the impact of dynamical friction on stellar motion using a series of two-dimensional simulations in a wind tunnel configuration. This study performs three-dimensional (3D) local simulations of a star with outflows embedded in an AGN disk using the shearing box approximation, which was initially introduced by Hawley et al. (1995) in the study of the magnetorotational instability, re-casting the equations of motion in a local Cartesian frame co-rotating with the disk at an arbitrary radius  $r_0$ . The validity of this approximation is maintained as long as the studied domain remains significantly smaller than  $r_0$ , making it a valuable tool for investigating local accretion disk dynamics (Balbus & Hawley 2003).

This paper is structured as follows. §2 outlines the numerical methods, disk model, and all simulated cases. §3 compares the effects of friction and anti-friction, analyzing the physical parameters that influence gas-star interactions. §4 presents a case study on the dynamical evolution of an sBH embedded in an AGN disk under the influence of anti-friction. Finally, §5 provides a discussion and summary of the results.

## 2. METHODS

This work uses the GPU-optimized higher-order Godunov code **Kratos** (Wang 2025), in simulation domains that consider shearing flows according to Keplerian mo-

**Table 2.** ALL simulated models in this work.

Series	Name	** $\langle a_y \rangle$ [10 <sup>-8</sup> km s <sup>-2</sup> ]	** $\langle \dot{r}_{\text{cir}} \rangle$ [km s <sup>-1</sup> ]	Description
Fiducial Studies <sup>†</sup>	FID <sup>+-</sup>	0.24	2.41	Fiducial model; $x_p = 90$ AU (§3.1)
	MASS <sup>+</sup>	-0.30	-2.96	$m = 80 M_\odot$ , $v_{\text{src}} = 2 \times 10^8$ cm s <sup>-1</sup> (§3.1)
	GAMMA <sup>+</sup>	0.08	0.79	$\gamma = 4/3$ (§3.5)
	PG-45 <sup>+-</sup>	0.77	7.59	$x_p = 45$ AU (§3.2)
	PG-0 <sup>+-</sup>	-0.37	-3.65	$x_p = 0$ AU (§3.2)
	JET-x <sup>+</sup>	-0.14	-1.38	Jet propagation along $\pm x$ (§3.3)
	JET-y <sup>+</sup>	-0.26	-2.56	Jet propagation along $\pm y$ (§3.3)
	JET-z <sup>+</sup>	-0.24	-2.36	Jet propagation along $\pm z$ (§3.3)
Case Study*	ACCD <sup>+-</sup>	0.11	1.1	Considering accretion disk (§3.4)
	BH-jet-z <sup>+</sup>	0.40	1.83	Considering a jet along $\pm z$ (§4)

NOTE—<sup>†</sup>:  $t_{\text{evo}} = 15$   $P$ . \*:  $t_{\text{evo}} = 0.1$   $P$ . \*\*: The time-averaged azimuthal acceleration  $\langle a_y \rangle$  and the mean rate of change of the orbital radius  $\langle \dot{r}_{\text{cir}} \rangle$  under the influence of anti-friction.<sup>+</sup>: Anti-friction cases where stars exhibit outflows (model names contain “-anti”). <sup>-</sup>: Friction cases where stars lack outflows (model names contain “-fric”).

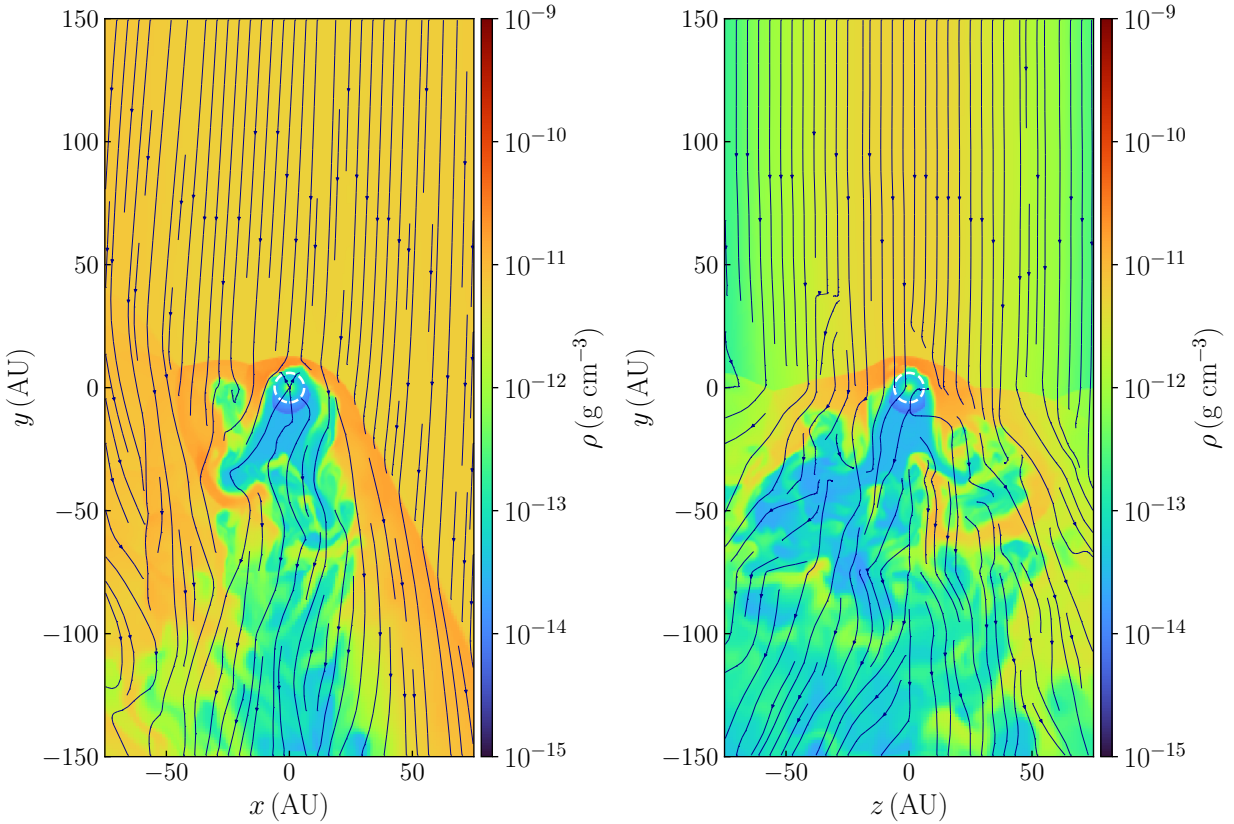


**Figure 1.** Gas density  $\rho$  in the  $z = 0$  plane (i.e., the orbital plane; left column) and the  $x = 0$  plane (right column) at the  $t_{\text{evo}} = 15$   $P$  snapshot of the fiducial model. The star is located at the origin, with color indicating gas density and black velocity streamlines representing the gas flow pattern. The white dashed circle indicates the characteristic standoff distance,  $R_0 \approx [\dot{m}v_{\text{src}}/(4\pi\rho_0 ||\mathbf{v}_g||^2)]^{1/2}$ , where the total pressure of the outflow balances that of the incoming ambient medium (Gruzinov et al. 2020; Li et al. 2020).

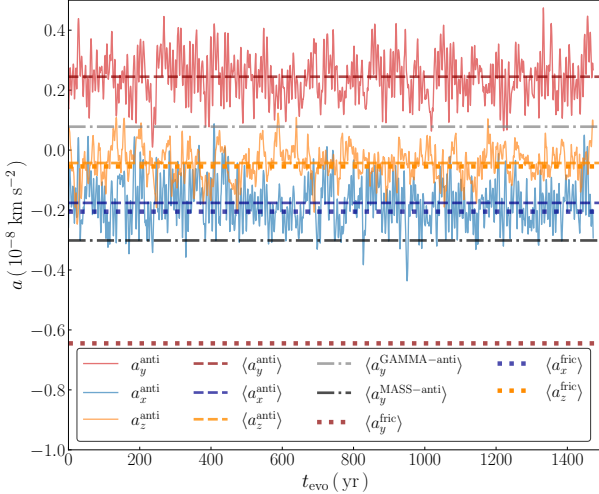


**Figure 2.** The acceleration experienced by the star in the FID-anti and FID-fric models. The red, blue, and orange lines represent the acceleration components in the  $x$ ,  $y$ , and  $z$  directions, respectively. Solid and dashed lines correspond to the FID-anti model, while the dotted lines represent the FID-fric model. The grey and black dash-dot lines represent the GAMMA-anti and MASS-anti models. The solid lines depict the instantaneous acceleration, whereas the other lines indicate the mean values over 15 orbital periods.

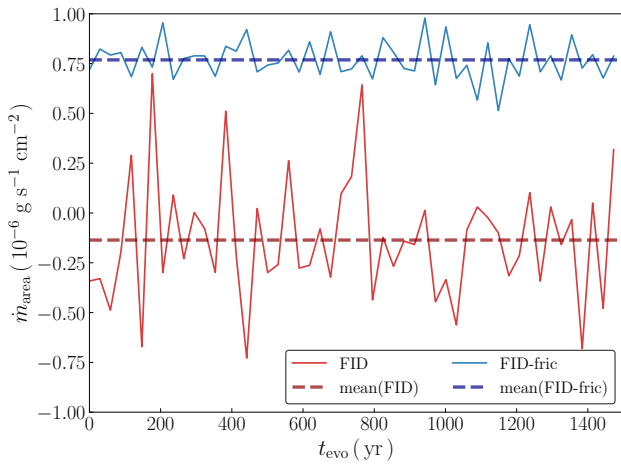


**Figure 3.** The mass accretion rate per area at  $x = -L_x$ . The red and blue lines correspond to the FID-anti and FID-fric models, respectively. The solid lines depict the instantaneous  $\dot{m}_{\text{area}}$ , while the dashed lines represent the mean values averaged over 15 orbital periods.

tion, to study the dynamical evolution of a star embedded in an AGN disk. Unless otherwise specified, all geometric-related physical quantities are defined in the shearing box reference frame. The coordinate system is Cartesian  $(x, y, z)$ , with  $x$  being radial,  $y$  being azimuthal, and  $z$  aligned with the AGN disk's rotation

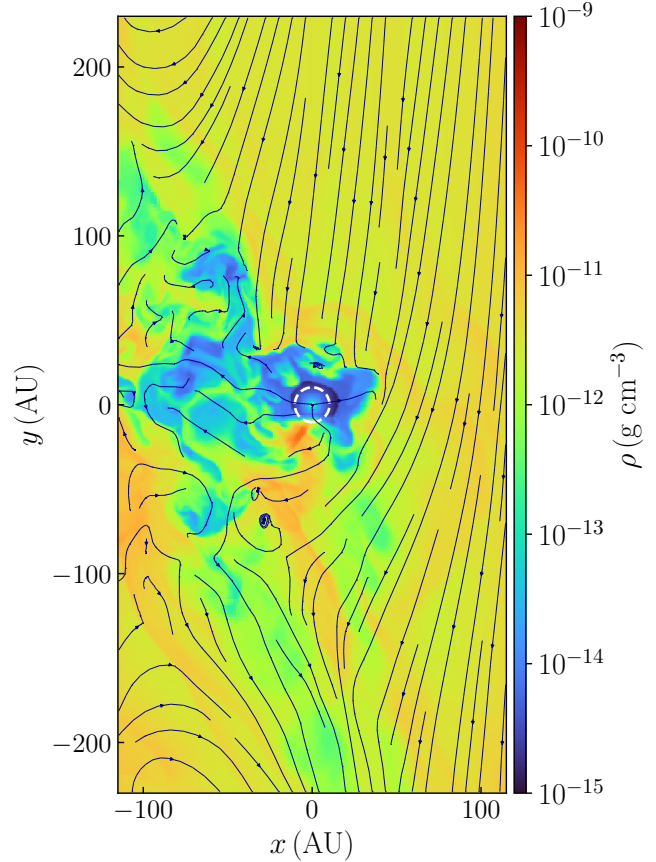


**Figure 4.** Similar to Figure 1, but for the MASS-anti model.

axis. The star is placed at the origin, while the SMBH is located on the negative  $x$ -axis at the disk center. The masses of the star and the SMBH are  $m$  and  $M$ , respectively, and both lie in the plane  $z = 0$ .

### 2.1. Dynamical Equations in the Shearing Box

As mentioned earlier, the local shearing box approximation uses a reference frame at a radius  $r_0$  (i.e., the location of the star), co-rotating with the disk at the orbital frequency  $\Omega(r_0) = \Omega_0 = \sqrt{GM/r_0^3}$  (Stone & Gardiner 2010). In this frame, the hydrodynamic (HD) equations are expressed in a Cartesian coordinate system  $(x, y, z)$  with unit vectors  $\hat{i}, \hat{j}, \hat{k}$ :

$$\begin{aligned}
 \partial_t \rho + \nabla \cdot (\rho \mathbf{v}) &= 0; \\
 \partial_t (\rho \mathbf{v}) + \nabla \cdot (\rho \mathbf{v} \mathbf{v} + p) &= \rho \Omega_0^2 (2q x \hat{i} - z \hat{k}) \\
 &\quad - 2\Omega_0 \hat{k} \times (\rho \mathbf{v}) - \rho \nabla \Phi_s - \rho f_{\text{acc}} \hat{j}; \\
 \frac{\partial E}{\partial t} + \nabla \cdot [\mathbf{v}(E + p)] &= \Omega_0^2 \rho \mathbf{v} \cdot (2q x \hat{i} - z \hat{k}) \\
 &\quad - \rho \mathbf{v} \cdot (\nabla \Phi_s + f_{\text{acc}} \hat{j}),
 \end{aligned} \tag{1}$$

where  $\rho$ ,  $\mathbf{v}$ ,  $p$  are gas density, velocity, and pressure, respectively. The shear parameter  $q \equiv -d \ln \Omega / d \ln r$  takes value  $q = 3/2$  for Keplerian rotation. Total energy density  $E$  is related to the pressure  $p$  and kinetic energy density by,

$$E = \frac{p}{\gamma - 1} + \frac{1}{2} \rho v^2, \quad (2)$$

where  $\gamma$  is the ratio of specific heats, and we take  $\gamma = 5/3$  throughout this work. The tangential acceleration  $f_{\text{acc}}$  is responsible of angular momentum removal that is associated with accretion processes, related to the radial accretion velocity  $v_{\text{acc}}$  via  $f_{\text{acc}} = -2\Omega_0 v_{\text{acc}}$ . Such parametrization focuses this work on the fundamental gas-star interactions without the complexity of detailed mechanisms that drive accretion. The gravitational potential of the star (not to be confused with the effective potential regarding the motion circulating the central blackhole) is  $\Phi_s$ . Such a central star is treated as a source particle (see e.g., [Murray et al. 2017](#)) that launches outflows. In order to consistently resolve the flow outside the source region ( $r_{\text{src}} < r \leq r_{\text{soft}}$ ) without excessively reducing the time step, the gravitational potential of the perturber is softened ([Dong et al. 2011](#)). Within this range, a fourth-order gravitational potential is applied,

$$\Phi_s^{(4)} = -GM_s \frac{r^2 + 1.5r_{\text{soft}}^2}{(r^2 + r_{\text{soft}}^2)^{3/2}}. \quad (3)$$

This work adopts  $r_{\text{soft}}/r_{\text{src}} \approx 3$  throughout all simulations. Following the approach in [Wang & Li \(2022\)](#), a spherical source region with a radius  $r_{\text{src}}$  is established around the star. When considering stellar outflows, an initial radial velocity  $v_{\text{src}}$  is set within the source region as a model parameter, and the density is adjusted to produce the desired mass-loss rate  $\dot{m} = 4\pi r^2 \rho v_{\text{src}}$ , where  $r^2 = x^2 + y^2 + z^2$ . The gas pressure is determined based on a typical temperature  $T_{\text{outflow}}$ . During the dynamical evolution, the physical quantities are fixed within the source region, ensuring constant outflows.

## 2.2. Basic Disk Model and Boundary Conditions

The 3D equilibrium AGN disk model is considered ([Nelson et al. 2013](#)). Since the validity of the shearing box approximation requires that the domain size be small relative to  $r_0$  ([Hawley et al. 1995](#)), the initial gas density  $\rho$  and pressure gradient  $\partial p / \partial x$  are assumed to be uniform in the  $x$ -direction, with a constant temperature  $T$  throughout the shearing box. The pressure gradient in the  $y$ -direction is assumed to be zero. The self-gravity of the gas is also neglected in this model, which is safe for the study focusing on the vicinity of stars embedded in AGN disks (see e.g. [Li & Lai 2022](#)).

Along the  $z$ -direction, the pressure gradient balances the gravitational force from the central SMBH,

$$-\frac{\partial p}{\partial z} - \rho \Omega_0^2 z = 0, \quad p = \frac{k_B T}{\mu m_p} \rho, \quad (4)$$

where  $m_p$  is the proton mass,  $\mu = 2.35$  is the mean molecular weight measured in  $m_p$ , and  $k_B$  is the Boltzmann constant. Solution to the vertical force balance yields,

$$\rho = \rho_0 \exp\left(-\frac{z^2}{2H_0^2}\right), \quad (5)$$

where  $\rho_0$  is the gas density at the  $z = 0$  plane,  $H_0 = c_{\text{iso}} / \Omega_0$  is the disk scale height, and  $c_{\text{iso}}^2 = p / \rho$  is the isothermal sound speed. The disk-only steady state of eq.(1) reads, in absence of the star,

$$\mathbf{v}_g = -q\Omega_0(x + x_p)\hat{j}, \quad x_p = -\frac{\partial_x p}{2q\Omega_0^2 \rho}, \quad (6)$$

which describes the uniform orbital motion of gas in the shearing box. We further introduce the parameter  $x_p$  for the offset between the orbiting body and the disk gas that moves with the same orbital velocity, caused by the presence of a radial pressure gradient in the disk ([Masset 2017](#)). For typical pressure profiles that decrease with radius,  $x_p > 0$  indicates that the tangential velocity of the object is greater than the ambient gas, resulting in a headwind.

More consistent thermodynamics is also a direction of potential improvements. This work assumes that the heating introduced by stellar outflows is negligible compared to the radiative cooling of the AGN disk. Taking the fiducial model as an example, the heating rate ratio  $\eta$  is estimated as

$$\begin{aligned} Q_{\text{kin}}^+ &\approx \frac{\dot{m} v_{\text{src}}^2}{2} \times \frac{1}{4\pi R_0^2} = \frac{\rho_0 \|\mathbf{v}_g\|^2}{2} v_{\text{src}}, \\ Q_{\text{rad}}^- &\equiv 2\sigma T_e^4 = 2\sigma T^4 \frac{\tau}{1 + \tau^2}, \\ \eta &= \frac{Q_{\text{kin}}^+}{Q_{\text{rad}}^-} \approx 10\% \times \left( \frac{\rho_0}{3.5 \times 10^{-11} \text{ g cm}^{-3}} \right) \\ &\times \left( \frac{\|\mathbf{v}_g\|}{4.1 \times 10^6 \text{ cm s}^{-1}} \right)^2 \times \left( \frac{v_{\text{src}}}{8 \times 10^7 \text{ cm s}^{-1}} \right) \\ &\times \left( \frac{T}{2.8 \times 10^4 \text{ K}} \right)^{-4}, \end{aligned} \quad (7)$$

where  $R_0 \approx [\dot{m} v_{\text{src}} / (4\pi \rho_0 \|\mathbf{v}_g\|^2)]^{1/2}$ ,  $Q_{\text{rad}}^-$  is the cooling rate due to radiative diffusion in the direction normal to the disk and  $\tau \approx H_0 \kappa_{\text{es}} \rho_0$  is the Rosseland mean opacity ([Hubeny 1990; Johnson & Gammie 2003; Jiang & Goodman 2011; Cantiello et al. 2021](#)). The above calculations

show that the kinetic heating from stellar outflow is insufficient to offset radiative cooling and maintain thermal equilibrium, even though turbulent heating alone has been found inadequate in the outer regions of AGN disks (Sirko & Goodman 2003; Thompson et al. 2005).

The size of the simulation box in this study is given by  $(-L_x, L_x) \times (-L_y, L_y) \times (-L_z, L_z)$ , where  $L_x, L_y, L_z$  represent the lengths in the  $x, y, z$ -directions, respectively. The BCs for the shearing box are set similarly to those in Dong et al. (2011). At the  $x$ -boundaries, the physical variables in the ghost zones are fixed at their unperturbed Keplerian values at  $x = \pm L_x$  (i.e., maintained in their initial state). Both sides of the  $x$ -boundaries allow waves to exit upon reaching the edges. For the  $y$ -boundaries, an inflow/outflow BC is applied. Variables in the ghost zones are fixed at their initial values at physical "inflow" boundaries ( $y < 0, x + x_p < 0$  and  $y > 0, x + x_p > 0$ ), and are copied from the last actively updated row of cells at physical "outflow" boundaries ( $y < 0, x + x_p > 0$  and  $y > 0, x + x_p < 0$ ). For the  $z$ -boundaries, a conventional outflow BC is used at  $z = \pm L_z$ .

### 2.3. Setup of Fiducial and Other Models

The fiducial model contains an  $8 M_\odot$  star embedded in the outer regions of an AGN disk, orbiting a central SMBH with a mass of  $10^8 M_\odot$ . The star generates isotropic outflows that interact with the ambient gas. For comparison, the star without outflows is also considered. The initial disk parameters and the definition of the outer region are adopted according to (Cantiello et al. 2021), with the outer region defined as the area where  $Q \equiv M/(\sqrt{8\pi\rho}r^3) \lesssim 1$ . In the fiducial model, the star is placed at a typical distance of  $r_0 = 5000 R_{\text{sch}} \approx 0.05$  pc, where  $R_{\text{sch}} \equiv 2GM/c^2$  is the Schwarzschild radius and  $c$  is the speed of light. It is noted that such radius approximately corresponds to the critical boundary separating the regions dominated and radiation-pressure-dominated regions (Cantiello et al. 2021). The star is assumed to reside in a gas-pressure-dominated region throughout this work. Other specific parameter settings are provided in Table 1.

Stars in AGN disks could be very massive with intense nuclear burning, many of which could reach the Eddington luminosity  $L_{\text{Edd}}$  (Cantiello et al. 2021). When the stellar luminosity exceeds the Eddington limit, intensive mass-loss is expected (e.g., Owocki & Shaviv 2012; Smith 2014). Following Paxton et al. (2011), this work assumes a super-Eddington outflow at the escape veloc-

ity  $v_{\text{esc}}$ ,

$$\begin{aligned} \dot{m} &= \frac{L_{\text{Edd}}}{v_{\text{esc}}^2}, \\ L_{\text{Edd}} &\equiv -\frac{4\pi Gmc}{\kappa}, z \\ &\approx 2.56 \times 10^5 \left(\frac{\kappa}{\kappa_{\text{es}}}\right)^{-1} \left(\frac{m}{8 M_\odot}\right) L_\odot, \\ v_{\text{esc}} &= \left(\frac{2Gm}{r_s}\right)^{1/2}, \end{aligned} \quad (8)$$

where  $\kappa$  is the opacity, with the electron-scattering  $\kappa_{\text{es}}$  value adopted.  $r_s$  is the stellar radius, which follows the approximate scaling relation  $r_s \propto m^{0.8}$  (Demircan & Kahraman 1991). The temperature of the stellar outflow is estimated based on the star's surface temperature (Cantiello et al. 2021). The outflow temperature,  $T_{\text{outflow}}$ , is expressed as:

$$T_{\text{outflow}} \equiv \left(T^4 + \frac{L_{\text{Edd}}}{4\pi r_s^2 \sigma}\right)^{1/4}, \quad (9)$$

where  $\sigma$  is the Stefan-Boltzmann constant.

In addition to the fiducial model, cases with different pressure gradients are explored in §3.2, anisotropic outflows ("jets") are studied in §3.3, and §3.4 and §4 study the specific cases where stars and sBHs are tested in accreting AGN disks. All models are summarized in Table 2, characterizing each model with the prescribed dynamical evolution time  $t_{\text{evo}}$ , the time-averaged acceleration along the  $y$ -axis  $\bar{a}_y$  under the effect of anti-friction, and the corresponding mean rate of change in orbital radius  $\dot{r}_{\text{cir}}$ . Following the approach of Dong et al. (2011), all the simulations run for several extra periods  $P$  before measuring the dynamical properties, excluding the influence of time-dependent structures on the star.

## 3. FIDUCIAL MODEL STUDIES

### 3.1. Gas-Star Interaction and Angular Momentum Transfer

Figure 1 illustrates the interactions between the star and disk gas for the fiducial model FID-anti, showing the density profile on the  $z = 0$  and  $x = 0$  planes at  $t_{\text{evo}} = 15 P$ . The pressure gradient leads to sub-Keplerian motion in the  $x + x_p > 0$  region, resulting in a headwind acting on the star. Combined with the star's outflow, this interaction gives rise to a bow shock structure on the leading side of the orbital motion, whose overdense in front of the moving star could lead to the anti-friction effect.

Figure 2 shows the time dependence of all three components of the star's acceleration, with dashed lines representing the mean values. The time average of the vertical component  $a_z$  is very close to zero, which is expected

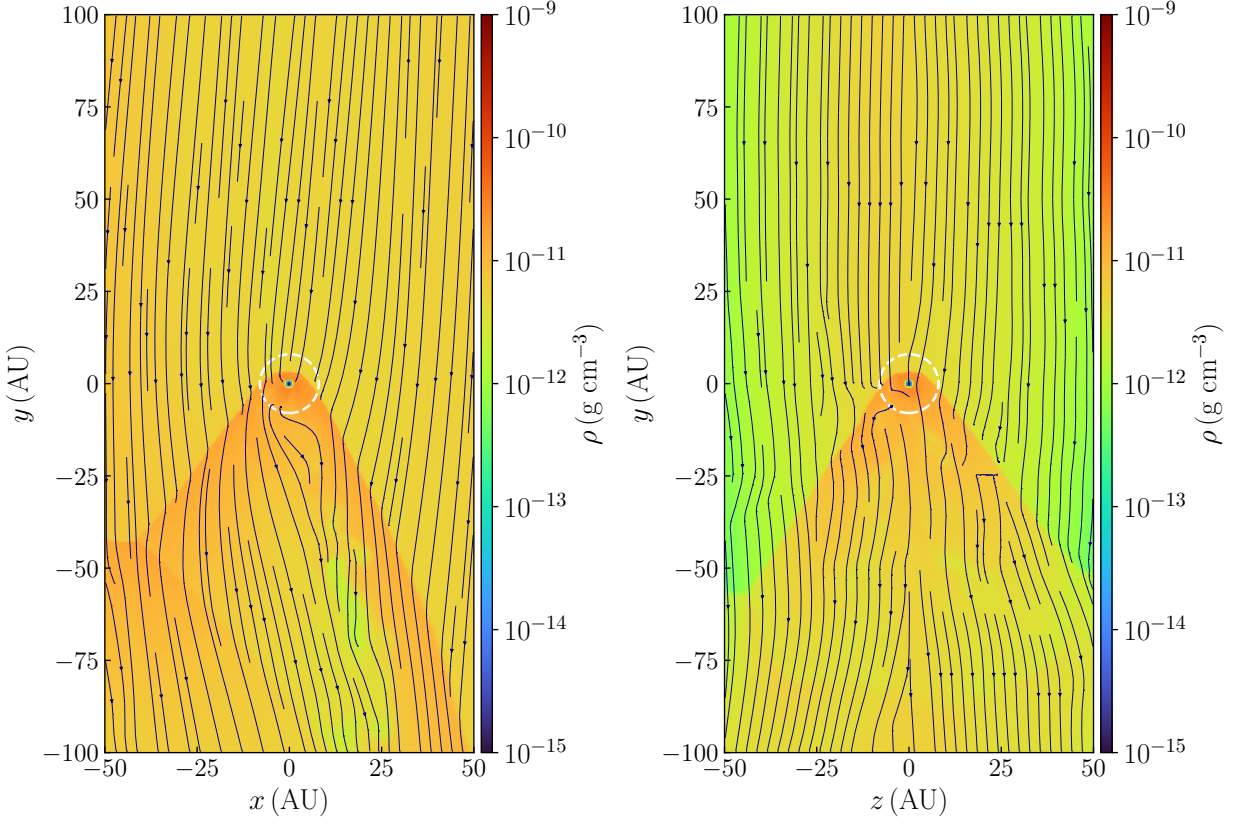


**Figure 5.** Similar to Figure 1, but for the star without outflow in the fiducial model. The white dashed circle indicates the Bondi radius,  $R_B = 2Gm/(c_{\text{iso}}^2 + \|\mathbf{v}_g\|^2)$ .

due to the reflection symmetry of the system. The  $a_y$  component, which dominates the orbital evolution due to angular momentum transfer, is positive because of the anti-friction. In the long run, the star is accelerated tangentially, moving outwards due to higher specific angular momentum caused by anti-friction. The asymmetry bow shock over the  $x$ -direction also induces a gravitational pull toward the central SMBH, yet the long-term effect of radial acceleration is negligible compared to tangential motion. Based on the Gauss planetary equations and the shearing box approximation, the evolution of the orbital radius  $r_{\text{cir}}$  reads,

$$\dot{r}_{\text{cir}} \approx \frac{2}{\Omega_0} a_y. \quad (10)$$

Quantitatively,  $\langle \dot{r}_{\text{cir}} \rangle \approx 2.4 \text{ km s}^{-1} > 0$ . Under the influence of anti-friction, the angular acceleration causes 1%  $v_0$  (where  $v_0 = \Omega_0 r_0$ ) acceleration within approximately 400 yr. Such acceleration is ultimately caused by the extraction of angular momentum from the disk gas, which should result in the enhancement of disk gas accretion. Figure 3 presents the mass accretion rate per unit area  $\dot{m}_{\text{area}}$  at  $x = -L_x$ , with the 15-period aver-

age being approximately  $-10^{-7} \text{ g s}^{-1} \text{ cm}^{-2}$  (where the negative value indicates accretion).

The case without stellar outflows is studied as the controlled group, keeping all other parameters unchanged, and is denoted as the FID-fric model. To reduce computational cost, the simulation box is reduced to  $(L_x, L_y, L_z) = (50, 100, 150)$  AU. Figure 5 presents the density profile at  $t_{\text{evo}} = 15 P$  for the FID-fric. Similar to the FID-anti model, the density wave remains symmetric about  $z = 0$  but asymmetric about  $x = 0$ . However, in this case, gas accumulates behind the moving star, forming an overdense wake that exerts a drag force, leading to dynamical friction. The dotted line for  $a_y$  in Figure 2 presents the acceleration of the star under dynamical friction, taking the opposite sign compared to the anti-friction case. Such comparison confirms that the anti-friction effect can flip the direction of orbit migration of stars embedded in AGN disk scenarios resulting in inward migration toward the disk center at a rate  $\langle \dot{r}_{\text{cir}} \rangle \approx -6.3 \text{ km s}^{-1}$ . In the meantime, the ambient gas gains angular momentum and the accretion is inhibited and even reverted as a decretion flow, as indicated by Figure 3.

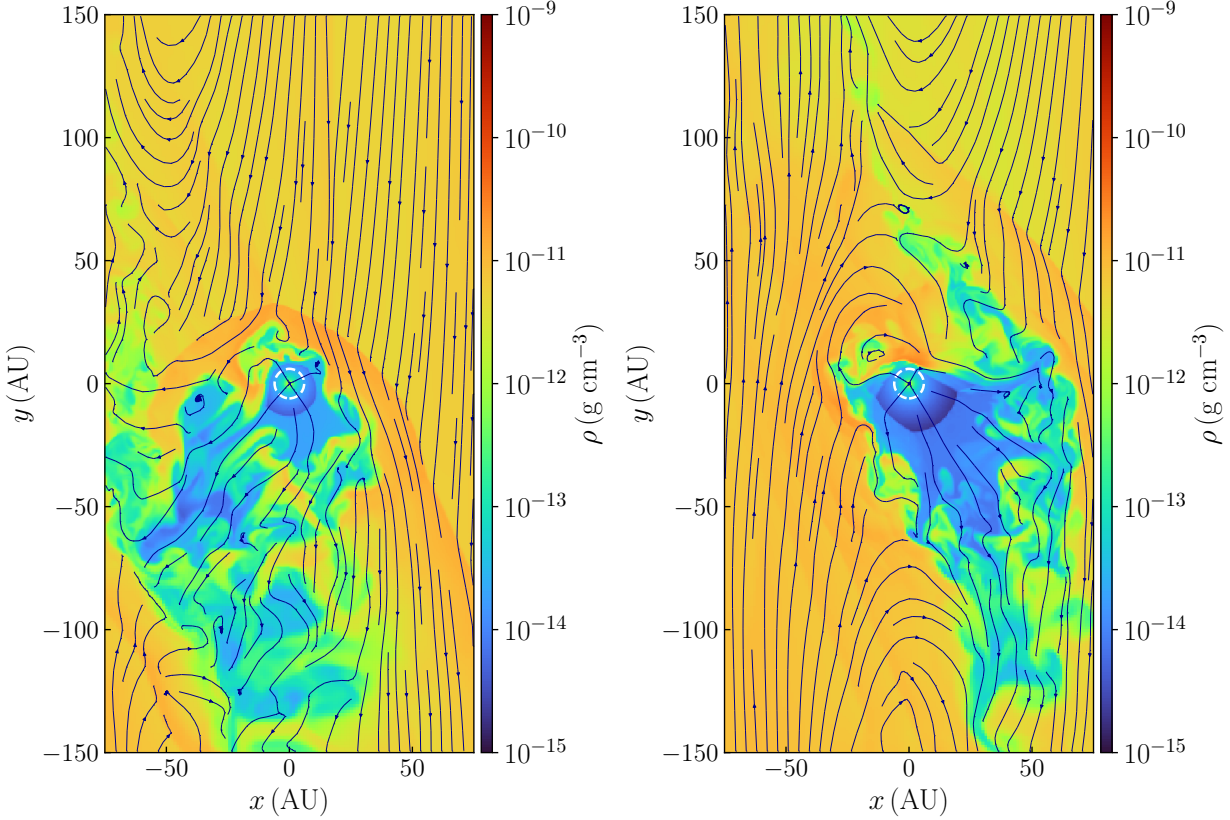


**Figure 6.** Gas density  $\rho$  in the  $z = 0$  plane (i.e., the orbital plane) at  $t_{\text{evo}} = 15 P$  for the PG-45 (left panel) and PG-0 (right panel) models. The white dashed circle indicates the characteristic standoff distance  $R_0$ .

Given that massive stars tend to yield higher mass-loss rates, an additional run simulates an  $80 M_{\odot}$  star, referred to as the MASS model. This case sets the outflow velocity to  $v_{\text{src}} = 2 \times 10^8 \text{ cm s}^{-1}$ , while other parameters remain identical to the fiducial model. As shown in Figures 2 through 4, the massive star experiences deceleration in the  $y$ -direction, in contrast to the acceleration observed in the FID-anti model. This difference arises mainly from the stronger gravitational concentration in the wake of the massive star on the ambient gas and the outflows outside the terminal shock, which leads to a more chaotic interaction between the outflow and the ambient gas that is dominated by the over-dense region on the trailing side.

### 3.2. Pressure Gradient

Both the FID-anti and FID-fric models identify that the radial distribution of tangential ( $y$ -component) velocity is key to the angular momentum acquisition. Because of the radial balance of force in the co-rotating frame (eq. 6), radial distribution of the relative gas velocity is primarily determined by the pressure gradient. Two additional models are hence introduced to explore the influence of radial pressure gradient, keeping

all other parameters of the FID-anti model intact. The parameter  $x_p$  is set to 45 AU and 0 AU, corresponding to models PG-45 and PG-0, respectively, where PG-0 represents a scenario where the radial pressure gradient vanishes, and greater  $x_p$  values indicates a steeper pressure gradient.

Figure 6 presents the density profiles in the orbital plane, showing the gas-star interactions of the PG-45 and PG-0 models. Compared to the FID-anti model, the gas density distribution in PG-45 and PG-0 exhibits increased irregularity due to stronger velocity shears. The reduced pressure gradient shifts the location where the gas velocity matches the orbital velocity, weakening the head-wind structure. The star accelerations in the PG-45 and PG-0 models are presented in Figure 7, showing distinct behaviors especially about the tangential component  $a_y$ . In the  $y$ -direction, the acceleration in PG-45 is higher than in the FID-anti model, because the magnitude of anti-friction is roughly inversely proportional to the relative velocity between the gas and the star (Li et al. 2020). In contrast, PG-0 exhibits significantly weaker anti-friction effect, which eventually yields a negative average  $\langle a_y \rangle$  even with outflows, due to the disrupted bow-shock structures.

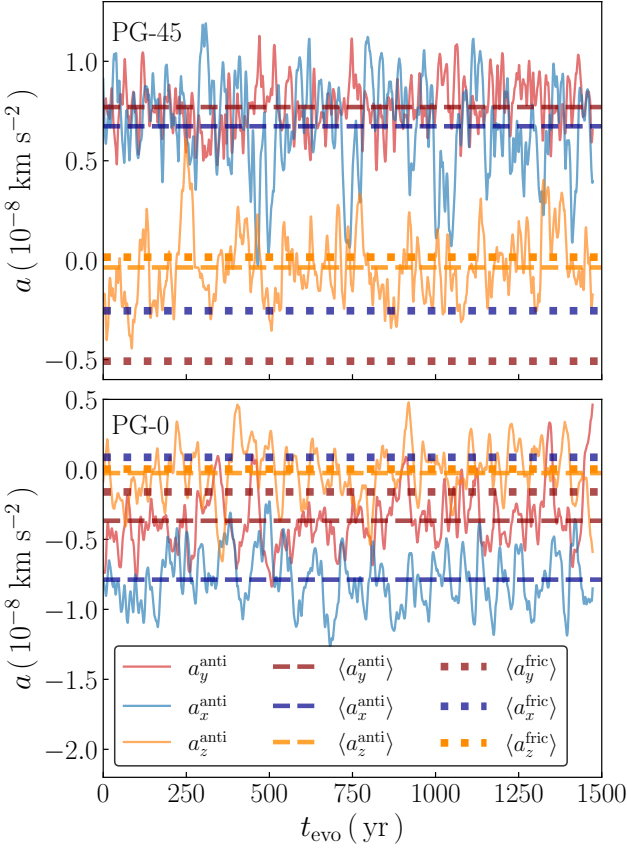


**Figure 7.** The acceleration experienced by the star in the PG-45 (upper panel) and PG-0 (lower panel) models. Both models include scenarios with and without stellar outflows.

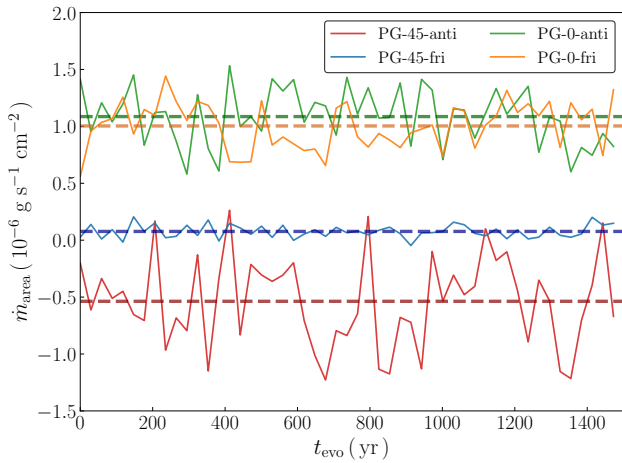


**Figure 8.** Similar to Figure 3, but for the PG-45 and PG-0 models.

Figure 8 shows that in PG-0, regardless of friction or anti-friction, the decretion onto the SMBH remains significant as the star loses angular momentum to the gas. PG-45, in contrast, exhibits consistently positive

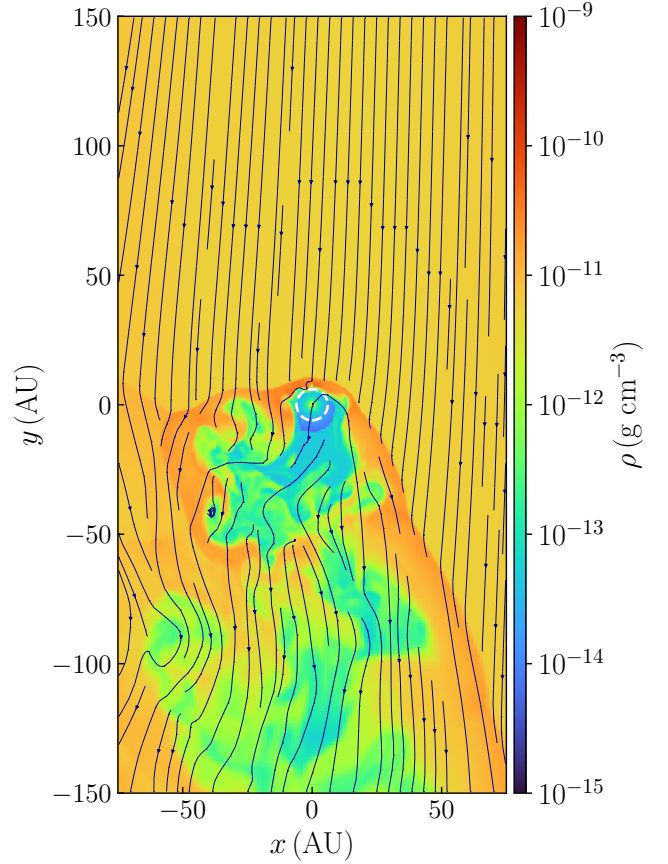


**Figure 9.** Similar to Figure 1, but for the GAMMA-anti model.

mean values for both  $a_x$  and  $a_y$  due to anti-friction, indicating the opposite direction of angular momentum transfer.

### 3.3. Anisotropic Outflow

If anisotropic outflows are launched from stars, the pattern of gas-star interactions might be significantly modified. Extra models are explored assuming jet-shaped stellar outflows, keeping all other parameters of the FID-anti model unchanged. The jets are launched along  $\pm x$ ,  $\pm y$ , and  $\pm z$  directions, corresponding to models marked as JET-x, JET-y, and JET-z, respectively. Jets are launched in collimation from both poles, whose mass flux are parameterized by  $\dot{m} = 2\pi r^2 \rho v_{\text{src}}$ .

Figures 10-11 illustrate the density distributions for gas-star interactions in all JET models. The JET-x and JET-z simulations behave similarly, in which jet outflows along the  $x$  and  $z$  directions create low-density regions on both sides of the star (with respect to  $x = 0$  or  $z = 0$ ), while the head-wind structure in the  $y$ -direction remains comparable to that in the FID-anti model. In both cases, the star experiences dynamical friction in

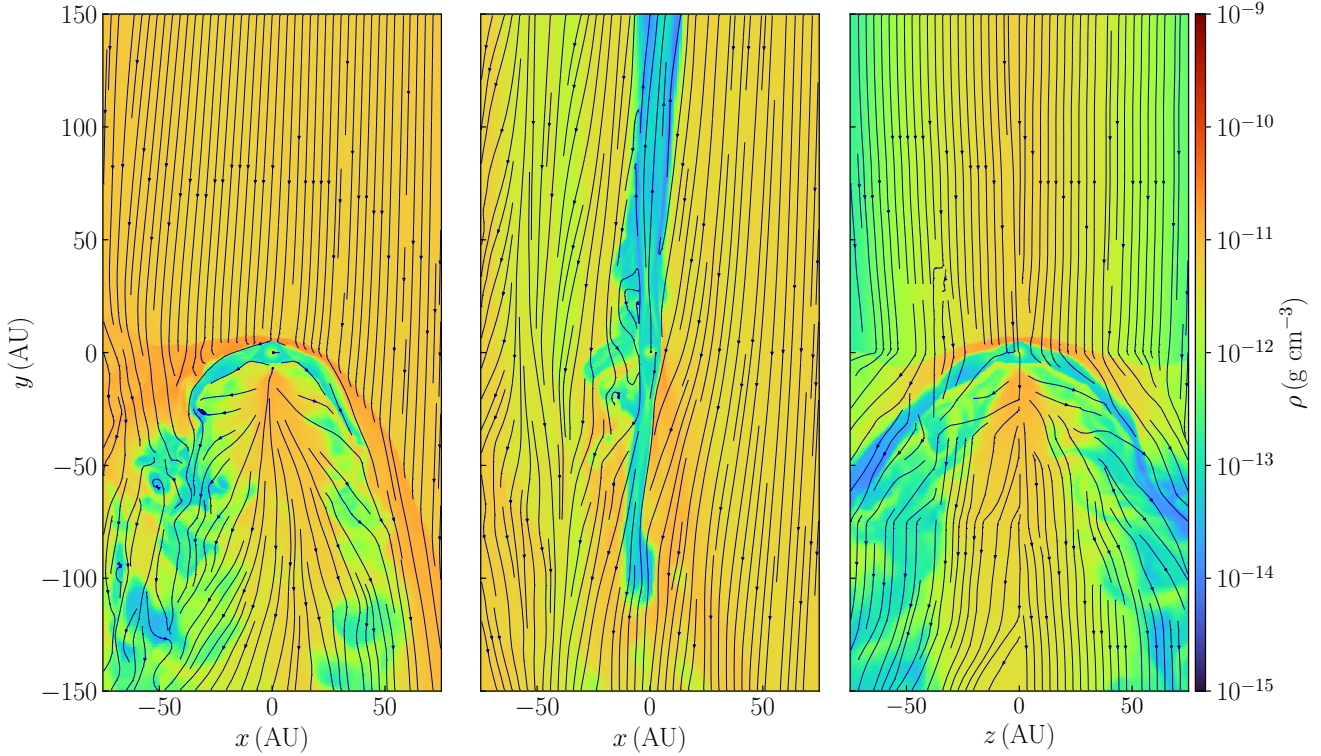


**Figure 10.** Similar to Figure 6, but for the JET-x (left panel), JET-y (middle panel), and JET-z (right panel) models.

the  $y$ -direction, indicating inward migration toward the disk center. In Model JET-x, the radial pressure gradient affects the symmetry of the interaction between the outflow and the ambient gas near  $x = 0$ . Such gradient suppresses the formation of the dense wake trailing the star, resulting in a weaker decelerating effect in the  $y$ -direction compared to the JET-z case. Due to the jet launched along the  $-x$  direction, the specific mass accretion rate  $\dot{m}_{\text{area}}$  at  $x = -L_x$  is negative (decretion). The time-averaged  $\dot{m}_{\text{area}}$  in the JET-z model is approximately zero. The JET-y model with strong  $y$ -outflows prevents the formation of an overdense region ahead of the star, effectively leading to a decelerating force in the  $y$ -direction. Since gas-star interaction in the JET-y model is primarily concentrated in the  $y$ -direction, the inflow effect on the gas along the  $x$ -direction is negligible, leading to an average  $\dot{m}_{\text{area}}$  at  $x = -L_x$  close to zero.

### 3.4. AGN Star in Accretion Disk

AGN disks are likely accreting. Using a representative accretion velocity  $v_{\text{acc}} = 10^6 \text{ cm s}^{-1}$ , Model ACCD simulate an outflowing star embedded in an accreting AGN disk. Figure 12 presents the density distribution in the ACCD model. Because of the significant  $v_x$  of disk gas towards the negative direction, the head-wind structure

becomes more aligned toward the disk center compared to the FID-anti model.

As Figure 13 shows, the star with outflows experiences acceleration in both the  $x$ - and  $y$ -directions due to anti-friction, resulting in rapid outward migration from the AGN disk. In disks with stronger accretion, the radial component of the anti-friction acceleration becomes increasingly significant, causing the AGN star's trajectory to align more closely with the radial direction. The orbital radius of the star expands at a rate of  $\langle \dot{r}_{\text{cir}} \rangle \approx 1.1 \text{ km s}^{-1}$ , which is comparable to the FID-anti model. In absence of stellar outflows, the star experiences dynamical friction from the ambient gas. The presence of accretion flow causes the star to experience acceleration in both the  $-x$  and  $-y$  directions. It is important to emphasize that the  $y$ -acceleration plays the dominant role in determining the orbital evolution of the star, while the influence of the  $x$ -acceleration is comparatively minor.

### 3.5. The GAMMA Model with $\gamma = 4/3$

The fiducial model assumes that the star resides near the boundary between the two regions dominated by gas pressure and radiation pressure, respectively. Given the fact that the outer disk is likely dominated by the radiation pressure, this sub-section simulates different cases adopting  $\gamma = 4/3$  instead of  $5/3$ , while keeping all

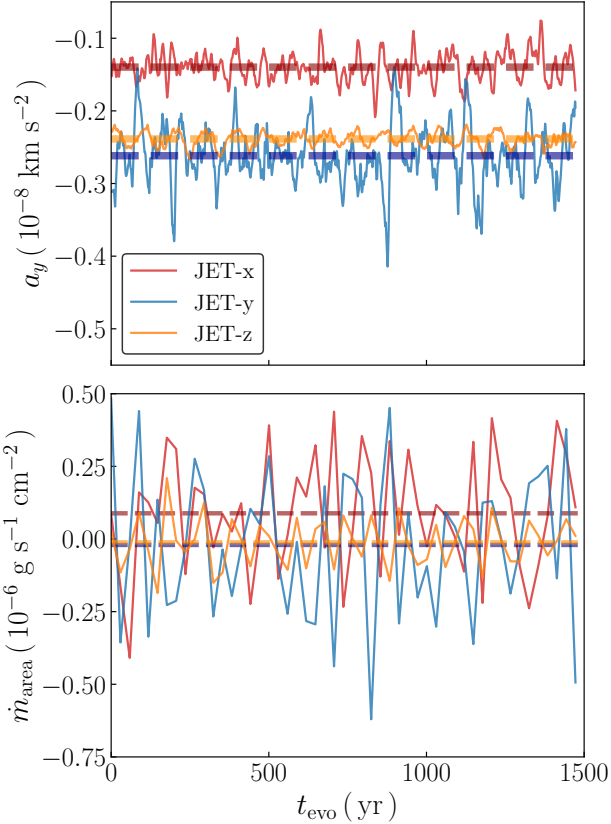


**Figure 11.** The star’s  $y$ -direction acceleration (upper panel) and the mass accretion rate per area at  $x = -L_x$  (lower panel) of JET-x, JET-y, and JET-z models. Both models consider the scenario with stellar outflow.

other parameters identical to the fiducial model. This case is hereafter referred to as the GAMMA model.

As shown in Figure 2, the GAMMA-anti model also undergoes acceleration due to anti-friction, although the magnitude is smaller than that in the FID-anti case. The comparison between Figures 1 and 9 indicates that the overdensity region leading the direction of motion is narrower in the GAMMA-anti model. A smaller  $\gamma$  value renders the ambient gas more susceptible to the stellar outflow, particularly near the contact discontinuity. This effect partially disrupts the formation of an overdense region ahead of the star, weakening the anti-friction-induced acceleration. The fundamental mechanism of the interactions between the stellar outflow and ambient gas remains unchanged, and hence the results are mostly changed quantitatively rather than qualitatively. The quantitative impact of such change will be revisited in §4.

#### 4. BLACK HOLE ORBIT DYNAMICS IN ACCRETION DISK

A type of extreme cases, which may be specifically interested by the studies on gravitational waves, involve sBHs with powerful outflows located at a distance of  $3000 R_{\text{sch}}$  from the center of a disk with significant accretion rate. Such simulation study, whose parameters are summarized in Table 3, have jet outflows aligned with the  $z$ -axis, and is referred to as BH-jet-z. The accretion disk is modeled by directly prescribing the velocity field of the disk gas.

Figure 14 presents a snapshot of the density distribution for the BH-jet-z model, whose impact of the sBH jet is distinct from the JET-z model. An underdense region forms behind the sBH along its direction of motion, associated with the jet launched along the  $z$ -axis. Because the sBH resides near the disk center, the high inflow velocity in the  $y$ -direction suppresses the initially bidirectional jet launched along the  $\pm z$ -axis, confining the jet material to the trailing side of the sBH. Under these conditions, the requirements for anti-friction are satisfied, and the sBH is accelerated in the  $y$ -direction by anti-friction. The time-averaged accelerations is  $\approx 0.40 \text{ km s}^{-2}$ , and the corresponding orbital radius evolution rate is  $\approx 1.83 \text{ km s}^{-1}$ .

Based on the above analysis, an intuitive picture of the sBH migration process can be proposed. If an sBH with jets along the  $z$ -axis is embedded in the outer region of an accretion disk, it would initially lose angular momentum due to dynamical friction and migrate inward toward the AGN disk center. As the sBH moves closer to the center, where the ambient gas density and inflow velocity are sufficiently high to confine the jet material to the trailing side of the sBH, the anti-friction effect in the azimuthal direction becomes effective. Consequently, the sBH gains angular momentum and transitions to outward migration. Under this interplay between inward and outward migration, the sBH is expected to eventually settle at an equilibrium location within the disk.

To explore the location of this trapped zone, a series of simulations was carried out by varying only the distance between the sBH and the disk center  $r_0$ , while keeping all other parameters identical to BH-jet-z model. The value of  $r_0$  is varied in the range of  $2000 - 5000 R_{\text{sch}}$  to identify the radius at which  $a_y = 0$ . The results are shown in Figure 15. As  $r_0$  increases, the acceleration from anti-friction is gradually suppressed, and beyond a certain distance, the anti-friction effect vanishes entirely. Three balance points are showed in the figure: the red and green points correspond to stable equilibrium, while the yellow point represents an unstable one.

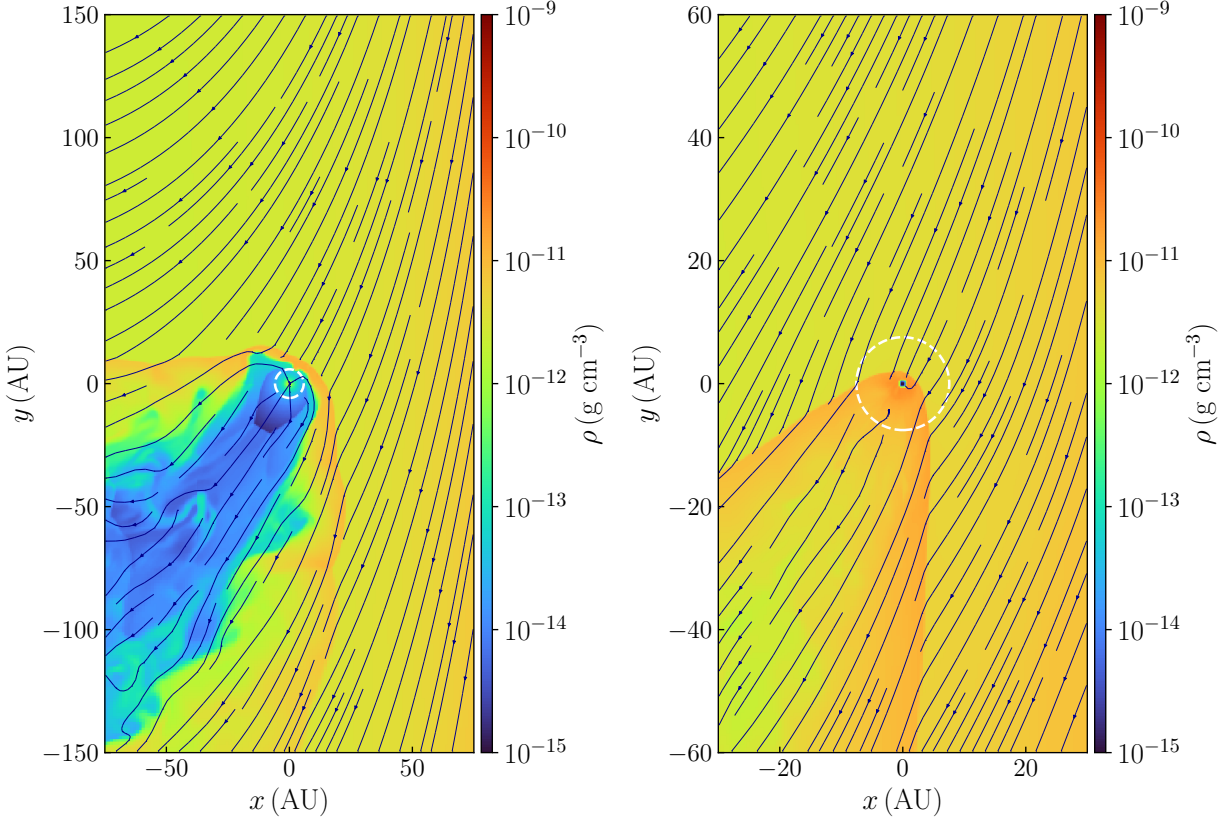


**Figure 12.** Similar to Figure 6, but for the ACCD-anti (left panel) and ACCD-fric (right panel) models. The white dashed circles indicate the characteristic standoff distance  $R_0$  in the left panel and the Bondi radius  $R_B$  on the right.

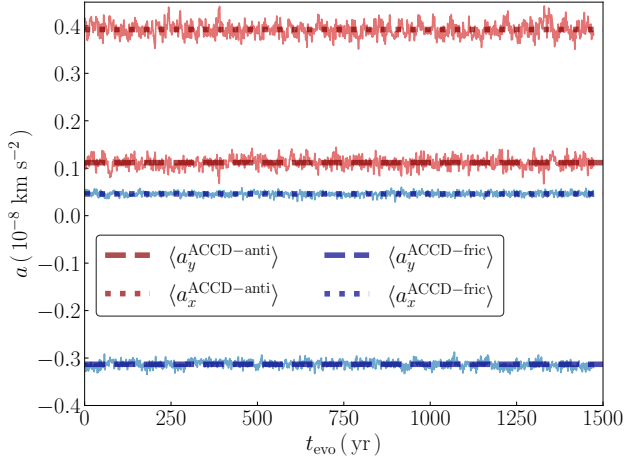


**Figure 13.** Similar to Figure 2, but for the ACCD-anti (red lines) and ACCD-fric (blue lines) models. The dashed lines represent acceleration in the  $y$ -direction, while the dotted lines represent acceleration in the  $x$ -direction.

Under the current parameter setup, the sBH is found to be trapped within the range of  $3808 - 4006 R_{\text{sch}}$ . The case with  $\gamma = 4/3$  is also examined, and the results show overall trends consistent with those shown in

Figure 15, though the trapped zone shifts much closer to the disk center. It is worth noting that, as discussed in §3, the sBH–gas interaction is also influenced by factors such as the radial pressure gradient and accretion velocity. Depending on the specific conditions, the sBH may either gain or lose angular momentum, resulting in outward migration or inward drift toward the disk center. The location of the trapped zone is also sensitive to parameter choices and may shift accordingly. These scenarios will be explored in future studies focusing on the parameters representing different astrophysical systems with detailed measurements.

## 5. DISCUSSION AND SUMMARY

This paper studies the dynamical evolution of stellar objects, including stars and black holes with outflows, located in the relatively outer region of AGN disks. In general, dynamical friction causes angular momentum loss, driving the AGN star toward the disk center. However, once the outflows satisfy some conditions that enables anti-friction, such stellar objects can gain angular momentum from the ambient gas instead, leading to an outward migration away from the AGN disk center.

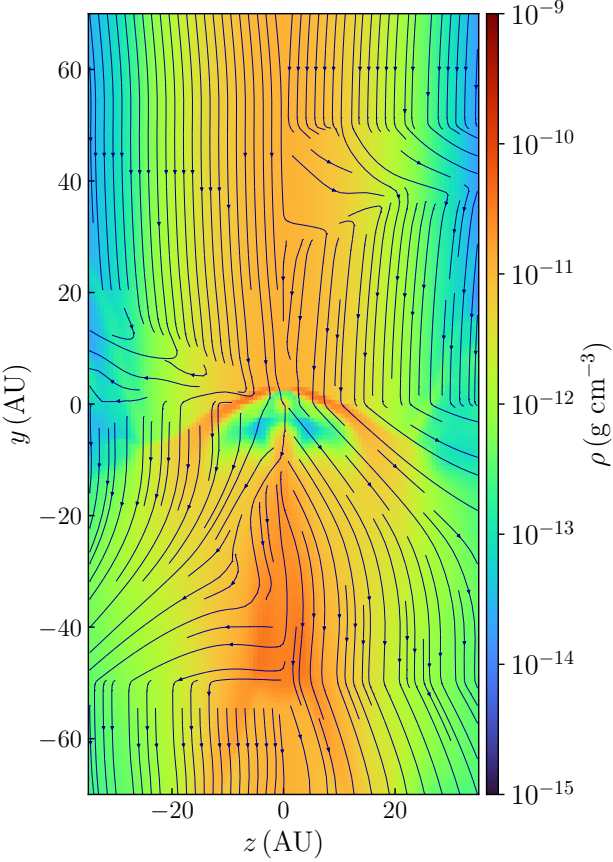


**Figure 14.** Gas density  $\rho$  in the  $x = 0$  plane at  $t_{\text{evo}} = 0.1 P$  for the BH-jet-z models.

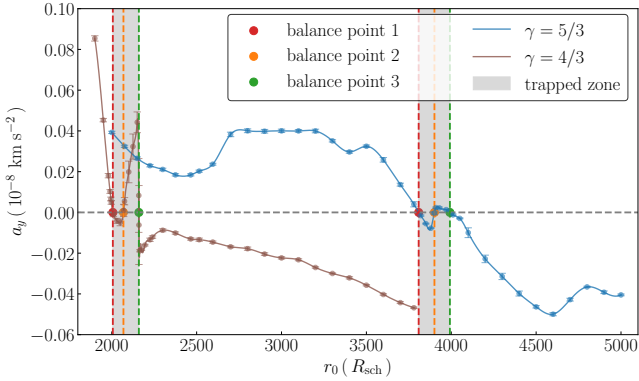


**Figure 15.** Time-averaged azimuthal acceleration of the SBH in the BH-jet-z models for different values of  $r_0$ .

### 5.1. Impacts of the Anti-friction on AGN Star Dynamical Evolution

Stars embedded within gaseous disks can excite spiral density waves, and the resulting net torque from the ambient gas, through dynamical friction, drives orbital migration. Depending on the stellar mass and the pres-

**Table 3.** Initial Properties of the BH-jet-z Models

Item	Value
<b>Disk Properties</b>	
$M$	$10^8 M_{\odot}$
$\rho_0$	$\sim 3.5 \times 10^{-11} \text{ g cm}^{-3}$
$c_{\text{iso}}$	$10^6 \text{ cm s}^{-1}$
$x_p$	90 AU
$v_{\text{acc}}^*$	$-1 \times 10^6 \text{ cm s}^{-1}$
<b>Stellar Properties</b>	
$m$	$10 M_{\odot}$
$r_0$	$3000 R_{\text{sch}}$
$\dot{m}$	$3 \times 10^{-3} M_{\odot} \text{ yr}^{-1}$
$T_{\text{outflow}}$	$\sim 5.7 \times 10^4 \text{ K}$
$v_{\text{src}}$	$1 \times 10^8 \text{ cm s}^{-1}$
$r_{\text{soft}}/r_{\text{src}}$	$\sim 3$
Outflow Type <sup>†</sup>	Jet
<b>Simulation Parameters</b>	
$L_x, L_y, L_z$	100, 200, 100 AU
Resolution ( $N_x, N_y, N_z$ )	128, 256, 128
$t_{\text{evo}}$	3 P

NOTE—<sup>\*</sup>: The negative sign indicates that the disk is undergoing accretion.

<sup>†</sup>: In the BH-jet-z model, the outflow is directed along the  $\pm z$  axis as a jet.

ence or absence of a gap in the ambient gas, migration has been classically categorized into three types: Type I, Type II, and Type III migration (Lin & Papaloizou 1979a,b, 1986; Ward 1986; Masset & Papaloizou 2003). Although dynamical friction has been extensively studied, the phenomenon of anti-friction has received comparatively little attention. It is also noted that, when supersonic outflows clear up a region surrounding the embedded star, the conclusions on the direction of orbital migration is more robust by getting rid of the subtleties in the star's vicinity that could be dominant in "traditional" studies of migration.

In a stable anti-friction scenario, the high-density region formed by the interaction between the stellar outflow and the ambient gas consistently remains ahead of the star's motion, while a low-density region persists behind it. This configuration enables AGN stars with sufficiently strong outflows to experience a more sustained and stable outward migration compared to those undergoing conventional migration mechanisms. The key factor in establishing anti-friction lies in the balance between the ram pressure of the stellar outflow and that of the ambient gas (Li et al. 2020). If the ambient gas density or velocity is too low or if the stellar outflow is excessively powerful, this balance cannot be achieved, and anti-friction fails to operate effectively. Consequently,

the strength of anti-friction is closely tied to the physical properties of the gas in the AGN disk, such as the radial pressure gradient.

Admittedly, there are several several caveats in this work related to the adopted stellar wind model, which should be addressed in future works. The stellar structure is simplified by modeling the star as a softened gravitational potential with artificially imposed outflows, without resolving realistic stellar envelopes. For the strong outflows at super-Eddington luminosities, two primary mechanisms are required, (1) additional energy release from the stellar interior, or (2) convective inefficiency near opacity bumps (Owocki et al. 2017; Owocki & Shaviv 2012). The first mechanism is difficult to sustain over long timescales, while a necessary condition for the second is that the opacity bump region be optically thick, which requires very massive stars. Even under optimistic assumptions for isolated stars, continuum-driven mass loss rates exceeding  $\sim 10^{-3} M_{\odot} \text{ yr}^{-1}$  are only possible when stellar masses exceed 40-60  $M_{\odot}$  (Cheng et al. 2024). Recent radiative hydrodynamic simulations indicate that for massive stars ( $\sim 50 M_{\odot}$ ) embedded in AGN-like environments, opacity-bump-induced mass loss is often suppressed by high accretion rates of  $\sim 0.01 M_{\odot} \text{ yr}^{-1}$  (Chen et al. 2024, 2025).

Accretion disks are vertically supported against the central gravitational force primarily by radial pressure gradients, which provide an upward force balancing gravitational compression (Shakura & Sunyaev 1973). This pressure support fundamentally determines the scale height and overall structure of the disk. In AGN disks, the dominant source of pressure varies with distance from the central black hole: radiation pressure dominates the innermost regions, whereas gas pressure and disk self-gravity become more critical at larger radii (Shapiro & Teukolsky 1986; Goodman 2003). These radial variations imply that the pressure gradient is not uniform and can feature localized maxima or sharp transitions. Recent studies, such as Jiang & Blaes (2020), have demonstrated that the iron opacity bump can increase the effective radiation pressure for a given vertical flux, resulting in the formation of pressure maxima within the disk. Variations in the radial pressure profile have significant dynamical implications for stars embedded in AGN disks. Specifically, the pressure gradient modulates the relative inflow velocity of ambient gas against the embedded star, which in turn influences the efficiency of anti-friction. This study investigates the role of the pressure gradient and finds that a weaker pressure gradient reduces the relative velocity between the star and the gas, thereby enhancing the anti-friction acceleration. However, if the pressure

gradient becomes too small to maintain a stable headwind structure around the star, the anti-friction effect is substantially suppressed, consequently hindering the outward migration of the AGN star.

More realistic AGN disk models should also emphasize turbulence as a key role in shaping disk gas dynamics. Turbulence driven by magnetorotational instability is an important candidate mechanism of angular momentum transfer and overall disk dynamics in various types of accretion disks (Balbus & Hawley 1998; Janiuk et al. 2004; Armitage 2011), whose resulting gas density fluctuations could possibly disrupt the spatial configurations of overdense and underdense regions around the concerned moving objects, potentially enhancing or suppressing the dynamical friction effect, either positive or negative. Such disturbances may introduce stochasticity into the orbital evolution of embedded stars. As this current work does not account for turbulences, future works shall incorporate a turbulent background to reflect realistic AGN disk conditions more consistently.

## 5.2. AGN sBH Migration

AGN disks have been recognized as promising environments for the formation of extreme mass ratio inspirals (EMRIs) (Bartos et al. 2017; Dittmann & Miller 2020; Pan et al. 2021; Pan & Yang 2021). Stellar-mass black holes (sBHs) can either originate from massive stars formed at the disk outskirts or be captured from the surrounding nuclear star cluster (Syer et al. 1991; Goodman & Tan 2004). Once embedded within the disk, sBHs may migrate inward toward the central SMBH due to various hydrodynamic effects, including density wave interactions (Artymowicz et al. 1993), thermal torques (Grishin et al. 2024), and head- or tailwind torques in geometrically thick disks (Chakrabarti 1993; Kocsis et al. 2011; Sánchez-Salcedo 2020). Those sBHs reaching sufficiently close to the SMBH can become EMRIs, and recent studies suggest that these wet EMRIs could contribute significantly to the overall cosmic EMRI population (Pan & Yang 2021; Pan et al. 2021; Derdzinski & Mayer 2023). Hydrodynamic and three-body simulations by Peng et al. (2024) further demonstrated that sBHs embedded in AGN disks can migrate in tandem with gap-opening intermediate-mass black holes (IMBHs), leading to sequential IMRI-IMRI formations or an EMRI event followed by an IMRI, highlighting the intricate interplay between migration and dynamical interactions.

This work reveals that, under the influence of anti-friction, sBHs can extract angular momentum from the ambient gas, initiating outward migration within the accretion disk. In extreme cases where the outflow forms a

strong jet, the sBHs could experience significant torque by azimuthal acceleration. If such an sBH initially migrates inward from the outer regions of the disk, the interplay between inward and outward migration could lead to its eventual trapping near an equilibrium radius. This dynamic process may result in the accumulation of multiple sBHs in these regions, promoting binary formation and ultimately leading to mergers.

### 5.3. Future Works

Due to the limitations in physical modeling, several caveats remain in this study that need further investigation in future works. The parameters adopted for all models were chosen as fixed representative values, which may not fully capture the diversity of the realistic scenarios. Future work should incorporate observational constraints to refine model setups. For the clarity of computation and analyses procedures, the approximation of adiabatic orbital evolution is adopted, in which the stellar orbit and mass are assumed to remain constant in the simulations, each of which represents one single snapshot. The dynamical evolution of stellar conditions, including mass, outflow intensity, and orbital radius, would provide more realistic results, especially when studying the anti-friction effects in global simulations. In global cases, perturbations in the stellar wake could traverse the entire orbital path and reinteract with the star itself, potentially altering the migration mechanism. Whether this feedback loop has a significant impact on AGN star migration remains uncertain, which is another interesting and important issue that worths further investigations.

Binary systems embedded in disks are also of possible interest, in which the physical scenario becomes substantially more complex. Previous studies, such as the series of works by Li & Lai (2022, 2023, 2024), have systematically examined the hydrodynamic evolution of stellar-

mass black hole binaries embedded in AGN disks, analyzing how various physical parameters influence their migration and eventual mergers. If both components of a binary system produce outflows, interactions between the two outflows, coupled with gas-star interactions, could significantly impact the binary's orbital evolution. For example, Wang & Li (2022) performed simulations of AGB star-outflowing pulsar systems and found that a dense and slow outflow can exert a positive torque on the binary. This torque leads to orbital expansion by more than 10%. It is therefore expected that binary evolution within AGN disks would also be strongly influenced by outflow-outflow interactions, which will be investigated in future work.

In addition, the types of astrophysical systems could extend far beyond this study, which primarily focuses on the impact of anti-friction on the AGN stars migration. Similar physical mechanisms may exist in other astrophysical scenarios. For instance, Liu et al. (2025) investigated the role of anti-friction in the migration of stars within open clusters. In environments such as protoplanetary disks, where the gas density is significantly lower than in AGN disks, the potential impact of anti-friction on planetary migration remains non-negligible if the planets are capable of generating sufficiently strong outflows. Future studies will extend the investigation of anti-friction to such systems.

## ACKNOWLEDGMENTS

M. Liu and L. Wang appreciates the computational resources provided by the Kavli Institute of Astronomy and Astrophysics at Peking University. We also thank our colleagues Ruobin Dong, Xian Chen, D. N. C. Lin, Xinyu Li and Erlin Qiao for helpful discussions and suggestions.

## REFERENCES

- Armitage, P. J. 2011, *ARA&A*, 49, 195, doi: [10.1146/annurev-astro-081710-102521](https://doi.org/10.1146/annurev-astro-081710-102521)
- Artymowicz, P., Lin, D. N. C., & Wampler, E. J. 1993, *ApJ*, 409, 592, doi: [10.1086/172690](https://doi.org/10.1086/172690)
- Balbus, S. A., & Hawley, J. F. 1998, *Reviews of Modern Physics*, 70, 1, doi: [10.1103/RevModPhys.70.1](https://doi.org/10.1103/RevModPhys.70.1)
- . 2003, in *Turbulence and Magnetic Fields in Astrophysics*, ed. E. Falgarone & T. Passot, Vol. 614, 329–348, doi: [10.48550/arXiv.astro-ph/0203353](https://doi.org/10.48550/arXiv.astro-ph/0203353)
- Bartos, I., Kocsis, B., Haiman, Z., & Márka, S. 2017, *ApJ*, 835, 165, doi: [10.3847/1538-4357/835/2/165](https://doi.org/10.3847/1538-4357/835/2/165)
- Cantiello, M., Jermyn, A. S., & Lin, D. N. C. 2021, *ApJ*, 910, 94, doi: [10.3847/1538-4357/abdf4f](https://doi.org/10.3847/1538-4357/abdf4f)
- Carrillo-Santamaría, J., López-Cámarra, D., De Colle, F., Moreno Méndez, E., & Sánchez-Salcedo, F. J. 2025, *MNRAS*, 540, 2952, doi: [10.1093/mnras/staf905](https://doi.org/10.1093/mnras/staf905)
- Chakrabarti, S. K. 1993, *ApJ*, 411, 610, doi: [10.1086/172863](https://doi.org/10.1086/172863)
- Chandrasekhar, S., & von Neumann, J. 1942, *ApJ*, 95, 489, doi: [10.1086/144420](https://doi.org/10.1086/144420)
- Chen, Y.-X., Jiang, Y.-F., & Goodman, J. 2025, *ApJ*, 987, 188, doi: [10.3847/1538-4357/addd0a](https://doi.org/10.3847/1538-4357/addd0a)
- Chen, Y.-X., Jiang, Y.-F., Goodman, J., & Lin, D. N. C. 2024, *ApJ*, 974, 106, doi: [10.3847/1538-4357/ad6dd4](https://doi.org/10.3847/1538-4357/ad6dd4)

- Chen, Y.-X., Jiang, Y.-F., Goodman, J., & Ostriker, E. C. 2023, *ApJ*, 948, 120, doi: [10.3847/1538-4357/acc023](https://doi.org/10.3847/1538-4357/acc023)
- Cheng, S. J., Goldberg, J. A., Cantiello, M., et al. 2024, *ApJ*, 974, 270, doi: [10.3847/1538-4357/ad701e](https://doi.org/10.3847/1538-4357/ad701e)
- Demircan, O., & Kahraman, G. 1991, *Ap&SS*, 181, 313, doi: [10.1007/BF00639097](https://doi.org/10.1007/BF00639097)
- Derdzinski, A., & Mayer, L. 2023, *MNRAS*, 521, 4522, doi: [10.1093/mnras/stad749](https://doi.org/10.1093/mnras/stad749)
- Dittmann, A. J., & Miller, M. C. 2020, *MNRAS*, 493, 3732, doi: [10.1093/mnras/staa463](https://doi.org/10.1093/mnras/staa463)
- Dong, R., Rafikov, R. R., Stone, J. M., & Petrovich, C. 2011, *ApJ*, 741, 56, doi: [10.1088/0004-637X/741/1/56](https://doi.org/10.1088/0004-637X/741/1/56)
- Edgar, R. 2004, *NewAR*, 48, 843, doi: [10.1016/j.newar.2004.06.001](https://doi.org/10.1016/j.newar.2004.06.001)
- Fabj, G., Nasim, S. S., Caban, F., et al. 2020, *MNRAS*, 499, 2608, doi: [10.1093/mnras/staa3004](https://doi.org/10.1093/mnras/staa3004)
- Goodman, J. 2003, *MNRAS*, 339, 937, doi: [10.1046/j.1365-8711.2003.06241.x](https://doi.org/10.1046/j.1365-8711.2003.06241.x)
- Goodman, J., & Tan, J. C. 2004, *ApJ*, 608, 108, doi: [10.1086/386360](https://doi.org/10.1086/386360)
- Grishin, E., Gilbaum, S., & Stone, N. C. 2024, *MNRAS*, 530, 2114, doi: [10.1093/mnras/stae828](https://doi.org/10.1093/mnras/stae828)
- Gruzinov, A., Levin, Y., & Matzner, C. D. 2020, *MNRAS*, 492, 2755, doi: [10.1093/mnras/staa013](https://doi.org/10.1093/mnras/staa013)
- Hawley, J. F., Gammie, C. F., & Balbus, S. A. 1995, *ApJ*, 440, 742, doi: [10.1086/175311](https://doi.org/10.1086/175311)
- Ho, L. C. 2008, *ARA&A*, 46, 475, doi: [10.1146/annurev.astro.45.051806.110546](https://doi.org/10.1146/annurev.astro.45.051806.110546)
- Hubeny, I. 1990, *ApJ*, 351, 632, doi: [10.1086/168501](https://doi.org/10.1086/168501)
- Janiuk, A., Czerny, B., Siemiginowska, A., & Szczerba, R. 2004, *ApJ*, 602, 595, doi: [10.1086/381159](https://doi.org/10.1086/381159)
- Jiang, Y.-F., & Blaes, O. 2020, *ApJ*, 900, 25, doi: [10.3847/1538-4357/aba4b7](https://doi.org/10.3847/1538-4357/aba4b7)
- Jiang, Y.-F., & Goodman, J. 2011, *ApJ*, 730, 45, doi: [10.1088/0004-637X/730/1/45](https://doi.org/10.1088/0004-637X/730/1/45)
- Johnson, B. M., & Gammie, C. F. 2003, *ApJ*, 597, 131, doi: [10.1086/378392](https://doi.org/10.1086/378392)
- Just, A., Yurin, D., Makukov, M., et al. 2012, *ApJ*, 758, 51, doi: [10.1088/0004-637X/758/1/51](https://doi.org/10.1088/0004-637X/758/1/51)
- Kennedy, G. F., Meiron, Y., Shukrgaliyev, B., et al. 2016, *MNRAS*, 460, 240, doi: [10.1093/mnras/stw908](https://doi.org/10.1093/mnras/stw908)
- Kocsis, B., Yunes, N., & Loeb, A. 2011, *PhRvD*, 84, 024032, doi: [10.1103/PhysRevD.84.024032](https://doi.org/10.1103/PhysRevD.84.024032)
- Kolykhalov, P. I., & Syunyaev, R. A. 1980, *Soviet Astronomy Letters*, 6, 357
- Levin, Y. 2003, arXiv e-prints, astro, doi: [10.48550/arXiv.astro-ph/0307084](https://doi.org/10.48550/arXiv.astro-ph/0307084)
- Li, R., & Lai, D. 2022, *MNRAS*, 517, 1602, doi: [10.1093/mnras/stac2577](https://doi.org/10.1093/mnras/stac2577)
- . 2023, *MNRAS*, 522, 1881, doi: [10.1093/mnras/stad1117](https://doi.org/10.1093/mnras/stad1117)
- . 2024, *MNRAS*, 529, 348, doi: [10.1093/mnras/stae504](https://doi.org/10.1093/mnras/stae504)
- Li, X., Chang, P., Levin, Y., Matzner, C. D., & Armitage, P. J. 2020, *MNRAS*, 494, 2327, doi: [10.1093/mnras/staa900](https://doi.org/10.1093/mnras/staa900)
- Lin, D. N. C., & Papaloizou, J. 1979a, *MNRAS*, 186, 799, doi: [10.1093/mnras/186.4.799](https://doi.org/10.1093/mnras/186.4.799)
- . 1979b, *MNRAS*, 188, 191, doi: [10.1093/mnras/188.2.191](https://doi.org/10.1093/mnras/188.2.191)
- . 1986, *ApJ*, 309, 846, doi: [10.1086/164653](https://doi.org/10.1086/164653)
- Liu, M., Wang, L., Fu, X., & Ho, L. C. 2025, *ApJ*, 978, 87, doi: [10.3847/1538-4357/ad91a9](https://doi.org/10.3847/1538-4357/ad91a9)
- Lynden-Bell, D. 1969, *Nature*, 223, 690, doi: [10.1038/223690a0](https://doi.org/10.1038/223690a0)
- MacLeod, M., & Lin, D. N. C. 2020, *ApJ*, 889, 94, doi: [10.3847/1538-4357/ab64db](https://doi.org/10.3847/1538-4357/ab64db)
- Masset, F. S. 2017, *MNRAS*, 472, 4204, doi: [10.1093/mnras/stx2271](https://doi.org/10.1093/mnras/stx2271)
- Masset, F. S., & Papaloizou, J. C. B. 2003, *ApJ*, 588, 494, doi: [10.1086/373892](https://doi.org/10.1086/373892)
- Murray, D. W., Chang, P., Murray, N. W., & Pittman, J. 2017, *MNRAS*, 465, 1316, doi: [10.1093/mnras/stw2796](https://doi.org/10.1093/mnras/stw2796)
- Nelson, R. P., Gressel, O., & Umurhan, O. M. 2013, *MNRAS*, 435, 2610, doi: [10.1093/mnras/stt1475](https://doi.org/10.1093/mnras/stt1475)
- Ostriker, E. C. 1999, *ApJ*, 513, 252, doi: [10.1086/306858](https://doi.org/10.1086/306858)
- Owocki, S. P., & Shaviv, N. J. 2012, in *Astrophysics and Space Science Library*, Vol. 384, *Eta Carinae and the Supernova Impostors*, ed. K. Davidson & R. M. Humphreys, 275, doi: [10.1007/978-1-4614-2275-4\\_12](https://doi.org/10.1007/978-1-4614-2275-4_12)
- Owocki, S. P., Townsend, R. H. D., & Quataert, E. 2017, *MNRAS*, 472, 3749, doi: [10.1093/mnras/stx2251](https://doi.org/10.1093/mnras/stx2251)
- Paczynski, B. 1978, *AcA*, 28, 91
- Pan, Z., Lyu, Z., & Yang, H. 2021, *PhRvD*, 104, 063007, doi: [10.1103/PhysRevD.104.063007](https://doi.org/10.1103/PhysRevD.104.063007)
- Pan, Z., & Yang, H. 2021, *PhRvD*, 103, 103018, doi: [10.1103/PhysRevD.103.103018](https://doi.org/10.1103/PhysRevD.103.103018)
- Panamarev, T., Shukrgaliyev, B., Meiron, Y., et al. 2018, *MNRAS*, 476, 4224, doi: [10.1093/mnras/sty459](https://doi.org/10.1093/mnras/sty459)
- Paxton, B., Bildsten, L., Dotter, A., et al. 2011, *ApJS*, 192, 3, doi: [10.1088/0067-0049/192/1/3](https://doi.org/10.1088/0067-0049/192/1/3)
- Peng, P., & Chen, X. 2023, *ApJ*, 950, 3, doi: [10.3847/1538-4357/acce3b](https://doi.org/10.3847/1538-4357/acce3b)
- Peng, P., Franchini, A., Bonetti, M., Sesana, A., & Chen, X. 2024, arXiv e-prints, arXiv:2411.16070, doi: [10.48550/arXiv.2411.16070](https://doi.org/10.48550/arXiv.2411.16070)
- Peterson, B. M. 1997, *An Introduction to Active Galactic Nuclei*
- Sánchez-Salcedo, F. J. 2020, *ApJ*, 897, 142, doi: [10.3847/1538-4357/ab9b2d](https://doi.org/10.3847/1538-4357/ab9b2d)
- Schmidt, M. 1963, *Nature*, 197, 1040, doi: [10.1038/1971040a0](https://doi.org/10.1038/1971040a0)
- Shakura, N. I., & Sunyaev, R. A. 1973, *A&A*, 24, 337

- Shapiro, S. L., & Teukolsky, S. A. 1986, Black Holes, White Dwarfs and Neutron Stars: The Physics of Compact Objects
- Shlosman, I., & Begelman, M. C. 1987, *Nature*, 329, 810, doi: [10.1038/329810a0](https://doi.org/10.1038/329810a0)
- Sirkov, E., & Goodman, J. 2003, *MNRAS*, 341, 501, doi: [10.1046/j.1365-8711.2003.06431.x](https://doi.org/10.1046/j.1365-8711.2003.06431.x)
- Smith, N. 2014, *ARA&A*, 52, 487, doi: [10.1146/annurev-astro-081913-040025](https://doi.org/10.1146/annurev-astro-081913-040025)
- Stone, J. M., & Gardiner, T. A. 2010, *ApJS*, 189, 142, doi: [10.1088/0067-0049/189/1/142](https://doi.org/10.1088/0067-0049/189/1/142)
- Syer, D., Clarke, C. J., & Rees, M. J. 1991, *MNRAS*, 250, 505, doi: [10.1093/mnras/250.3.505](https://doi.org/10.1093/mnras/250.3.505)
- Thompson, T. A., Quataert, E., & Murray, N. 2005, *ApJ*, 630, 167, doi: [10.1086/431923](https://doi.org/10.1086/431923)
- Wang, J.-M., Liu, J.-R., Ho, L. C., & Du, P. 2021, *ApJL*, 911, L14, doi: [10.3847/2041-8213/abee81](https://doi.org/10.3847/2041-8213/abee81)
- Wang, L. 2025, *ApJS*, 277, 63, doi: [10.3847/1538-4365/adbdb6](https://doi.org/10.3847/1538-4365/adbdb6)
- Wang, L., & Li, X. 2022, *ApJ*, 932, 108, doi: [10.3847/1538-4357/ac6ce6](https://doi.org/10.3847/1538-4357/ac6ce6)
- Wang, Y., Zhu, Z., & Lin, D. N. C. 2024, *MNRAS*, 528, 4958, doi: [10.1093/mnras/stae321](https://doi.org/10.1093/mnras/stae321)
- Ward, W. R. 1986, *Icarus*, 67, 164, doi: [10.1016/0019-1035\(86\)90182-X](https://doi.org/10.1016/0019-1035(86)90182-X)